are different and reflect the respective mobilities, with the highest being along the *b* and *c* axes, in agreement with the calculated lighter effective masses along these axes. The distinctive crystal structure of SnSe, therefore, plays a key role in the exceptional electronic band structure characteristics that result in an ultrahigh *PF* and *ZT*. The 2D sheets in SnSe have strong, accordion-like corrugation and are well separated from one another, with long intersheet Sn···Se bonding interactions of ~3.5 Å (Fig. 4). Longer Sn-Se bonding interactions of ~3.3 Å are also present along the corrugation direction (*c* axis). Along the *c* and *b* directions, the Sn-Se bonding is shorter, at 3.3 and 2.8 Å, respectively. As a result, the width of the valence bands along these in-plane directions is wider (and the effective hole masses lower) than along the *a* direction (lower carrier mobilities and larger effective hole masses).

We demonstrate that hole doping SnSe pushes its Fermi level deep into the band structure, activating multiple valence band maxima that lie close together in energy, enabling enhanced Seebeck coefficients and power factors (*PF*s). Therefore, the unique electronic band structure of SnSe is key to the high power factor and thermoelectric performance of the doped samples over a wide temperature plateau, from 300 to 773 K. The high conversion efficiency improves the prospects of realizing very efficient thermoelectric devices with hole-doped SnSe crystals as a p-type leg.

REFERENCES AND NOTES

1. L. E. Bell, *Science* **321**, 1457–1461 (2008).
2. J. P. Heremans, M. S. Dresselhaus, L. E. Bell, D. T. Morelli, *Nat. Nanotechnol.* **8**, 471–473 (2013).
3. X. Zhang, L. D. Zhao, *J. Materiomics* **1**, 92–105 (2015).
4. M. S. Dresselhaus *et al.*, *Adv. Mater.* **19**, 1043–1053 (2007).
5. L. D. Zhao, V. P. Dravid, M. G. Kanatzidis, *Energy Environ. Sci.* **7**, 251–268 (2014).
6. K. F. Hsu *et al.*, *Science* **303**, 818–821 (2004).
7. B. Poudel *et al.*, *Science* **320**, 634–638 (2008).
8. M. Zhou, J. F. Li, T. Kita, *J. Am. Chem. Soc.* **130**, 4527–4532 (2008).
9. K. Biswas *et al.*, *Nature* **489**, 414–418 (2012).
10. P. F. R. Poudeu *et al.*, *Angew. Chem. Int. Ed.* **45**, 3835–3839 (2006).
11. J. P. Heremans *et al.*, *Science* **321**, 554–557 (2008).
12. Y. Pei *et al.*, *Nature* **473**, 66–69 (2011).
13. W. Liu *et al.*, *Phys. Rev. Lett.* **108**, 166601 (2012).
14. H. Z. Zhao *et al.*, *Nano Energy* **7**, 97–103 (2014).
15. L. D. Zhao *et al.*, *J. Am. Chem. Soc.* **135**, 7364–7370 (2013).
16. X. Shi *et al.*, *J. Am. Chem. Soc.* **133**, 7837–7846 (2011).
17. M. M. Nassary, *Turk. J. Phys.* **33**, 201–208 (2009).
18. L. D. Zhao *et al.*, *Nature* **508**, 373–377 (2014).
19. Y. I. Ravich, B. A. Efimova, I. A. Smirnov, *Semiconducting Lead Chalcogenides* (Plenum, New York, 1970), vol. 5.
20. S. I. Kim *et al.*, *Science* **348**, 109–114 (2015).
21. S. K. Placheova, *Phys. Status Solidi (a)* **83**, 349–355 (1984).
22. G. J. Snyder, in *Thermoelectrics Handbook: Macro to Nano*, D. M. Rowe, Ed. (CRC/Taylor and Francis, Boca Raton, FL, 2006), chap. 9.
23. H. J. Wu *et al.*, *Nat. Commun.* **5**, 4515 (2014).
24. D. M. Rowe, *CRC Handbook of Thermoelectrics* (CRC Press, London, 1995).
25. C. W. Li *et al.*, *Nat. Phys.* **11**, 1063–1069 (2015).
26. F. Serrano-Sánchez *et al.*, *Appl. Phys. Lett.* **106**, 083902 (2015).
27. Q. Zhang *et al.*, *Adv. Energy Mater.* **5**, 1500360 (2015).
28. H. Wang, Y. Pei, A. D. LaLonde, G. J. Snyder, *Adv. Mater.* **23**, 1366–1370 (2011).
29. L. D. Zhao *et al.*, *J. Am. Chem. Soc.* **134**, 7902–7912 (2012).
30. G. Tan *et al.*, *J. Am. Chem. Soc.* **136**, 7006–7017 (2014).
31. Y. Pei, H. Wang, G. J. Snyder, *Adv. Mater.* **24**, 6125–6135 (2012).
32. G. Shi, E. Kioupakis, *J. Appl. Phys.* **117**, 065103 (2015).
33. Details of the calculations are available as supplementary materials on *Science* Online.
34. C. L. Chen, H. Wang, Y. Y. Chen, T. Day, G. J. Snyder, *J. Mater. Chem. A* **2**, 11171–11176 (2014).
35. S. Sassi *et al.*, *Appl. Phys. Lett.* **104**, 212105 (2014).

ACKNOWLEDGMENTS

This work was supported in part by the U.S. Department of Energy, Office of Science and Office of Basic Energy Sciences, under award DE-SC0014520 (G.T., H.C., V.P.D., S.H., C.W., and M.G.K.); and S3TEC-EFRC grant DE-SC0001299 (G.J.S.). This work was also supported by the "Zhuoyue" Program from Beihang University and the Recruitment Program for Young Professionals and the National Natural Science Foundation of China under grant 51571007 (L.-D.Z., Y.P., S.G., and H.X.). and by the Science, Technology and Innovation Commission of Shenzhen Municipality under grant no. ZDSYS20141118160434515 and Guangdong Science and Technology Fund under grant no. 2015A030308001 (J.H.). The synthesis, characterization, transport measurements, and DFT calculations were supported by DE-SC0014520. The validation measurements were supported by DE-SC0001299. Measurements at University of Michigan (C.U.) were supported by Energy Frontier Research Centers (EFRC) grant DE-SC0001054. All data in the main text and the supplementary materials are available online at www.sciencemag.org.

SUPPLEMENTARY MATERIALS

www.sciencemag.org/content/351/6269/141/suppl/DC1
Materials and Methods
Supplementary Text
Figs. S1 to S13
References (*36*–*47*)

3 September 2015; accepted 12 November 2015
Published online 26 November 2015
10.1126/science.aad3749

GEOPHYSICS

Shear deformation of bridgmanite and magnesiowüstite aggregates at lower mantle conditions

Jennifer Girard, George Amulele,* Robert Farla,† Anwar Mohiuddin, Shun-ichiro Karato‡

Rheological properties of the lower mantle have strong influence on the dynamics and evolution of Earth. By using the improved methods of quantitative deformation experiments at high pressures and temperatures, we deformed a mixture of bridgmanite and magnesiowüstite under the shallow lower mantle conditions. We conducted experiments up to about 100% strain at a strain rate of about 3×10^{-5} second^{-1}. We found that bridgmanite is substantially stronger than magnesiowüstite and that magnesiowüstite largely accommodates the strain. Our results suggest that strain weakening and resultant shear localization likely occur in the lower mantle. This would explain the preservation of long-lived geochemical reservoirs and the lack of seismic anisotropy in the majority of the lower mantle except the boundary layers.

Earth's large, rocky lower mantle is mostly composed of $(Mg,Fe)SiO_3$ bridgmanite (~70%) and (Mg,Fe)O magnesiowüstite (~20%) (and a few percent of calcium perovskite $CaSiO_3$) [e.g., (*1*)]. Many of Earth's geochemical and geophysical questions depend strongly on the rheological properties of materials in this region. For instance, geochemical observations suggest that the lower mantle hosts a large amount of incompatible elements working as a reservoir of these elements (*2*, *3*). The degree of preservation of these reservoirs is controlled by the nature of mixing or stirring of materials (*4*, *5*), which strongly depends on the rheological properties of materials in this region. However, very little is currently known about the rheological properties of materials in the lower mantle because of the difficulties in quantitative experimental studies of deformation under the conditions of the lower mantle.

Department of Geology and Geophysics, Yale University, New Haven, CT, USA.
*Present address: Department of Earth and Planetary Sciences, Macquarie University, Sydney, NSW, Australia. †Present address: Bayerisches Geoinstitut, Universität Bayreuth, Bayreuth, Germany.
‡Corresponding author. E-mail: shun-ichiro.karato@yale.edu

The main difficulties include the controlled generation of stress (or strain rate) and reliable measurements of stress and strain under the high-pressure and -temperature conditions [e.g., (*6*)]. Consequently, previous studies on plastic deformation of lower mantle minerals were either performed at high pressures and low temperatures (*7*–*10*), at high pressures and high temperatures without stress-strain rate control (*11*), or on analog materials at low pressures (*12*–*14*). Applying low-temperature experiments to Earth's interior is difficult because rheological properties are highly sensitive to temperature. Also the mechanisms by which deformation occurs are sensitive to temperature and strain rate, creating extrapolation issues for both low-temperature and poorly controlled strain-rate (stress) measurements [e.g., (*15*)]. Furthermore, microstructural evolution often leads to strain-dependent rheological behavior, which is particularly important for a sample containing two materials with a large strength contrast (*16*). The lower mantle approximates a two-phase mixture (bridgmanite and magnesiowüstite) with presumably a large strength contrast [e.g., (*13*, *17*, *18*)], and therefore large strain (>30%) experiments are essential to

characterize the evolution of rheological behavior of the lower mantle.

We performed large strain deformation experiments on a mixture of bridgmanite and magnesiowüstite by using the rotational Drickamer apparatus (*19*) at the synchrotron x-ray radiation facility (fig. S1). We have made several technical developments on the cell assembly (Fig. 1) and anvil design to increase the maximum pressure and to improve the quality of x-ray signals and performed quantitative deformation experiments under the conditions of the shallow lower mantle of Earth.

We prepared starting materials (ringwoodite or bridgmanite and magnesiowüstite) from San Carlos olivine by using the Kawai-type multianvil press. We carried out in situ deformation experiments at the shear strain rate of ~3×10^{-5} s^{-1} on lower mantle mineral mixtures at pressures at 24 to 27.5 GPa and temperatures up to 2000 to 2150 K (Table 1). All the deformed samples are a mixture of bridgmanite and magnesiowüstite with 1:1 mole ratio (~70:30 volume ratio). We estimated the pressure and temperature conditions by in situ x-ray diffraction data using the equations of state of bridgmanite and magnesiowüstite. We also estimated stress from radial x-ray diffraction and strain from x-ray image analysis of a Pt strain marker sandwiched vertically between two half rings of the sample (Fig. 1).

Stress increases with strain, initially achieving nearly steady state at strains higher than ~40%, with some hint of strain weakening for bridgmanite (Fig. 2). Because of a small sample size, the intensity of diffraction peaks is relatively weak, and we were able to determine the stress only from a limited number of diffraction planes. We used (110) and (112) planes for bridgmanite and (220) and (200) planes for magnesiowüstite. We took an arithmetic average of stress values from different planes to estimate the strength of each material. This is a crude way to estimate the strength of a polycrystalline material, but the precise relation between the strength of various slip systems and the average strength of an aggregate is not known [e.g., (*20*)]. Although the errors in the estimated stress are large, the results show that bridgmanite is likely substantially stronger than magnesiowüstite.

The microstructures of the deformed samples show evidence of substantial plastic deformation in both bridgmanite and magnesiowüstite (Fig. 3). Magnesiowüstite is isolated in most cases, whereas we infer bridgmanite to be interconnected on the basis of two-dimensional cross-sectional images. A large amount of strain accommodation by magnesiowüstite is evident from Fig. 3B, because magnesiowüstite is deformed more than the bulk strain. This is consistent with the conclusion drawn from the strength determination (Fig. 2). Our observations provide direct experimental verification that bridgmanite is substantially stronger than magnesiowüstite (*13*, *17*, *18*).

An obvious consequence of such a large rheological contrast is the evolution of strain partitioning with increasing strain, which may lead to shear localization [e.g., (*16*, *21*)]. Shear localization would limit substantial deformation to only in or near the boundary layers. Hence, stirring and mixing would occur selectively in these regions, with the rest of the lower mantle deforming very little. Relatively undeformed regions in the lower mantle, where little mass transport takes place, may act as long-lived geochemical reservoirs suggested by geochemical studies [e.g., (*2*, *5*)]. The possible localized deformation would also provide an alternative explanation for the absence of seismic anisotropy in the majority of the lower mantle other than the model proposed by Karato *et al.* (*22*), in which they attributed the absence of anisotropy in the majority of the lower mantle to the operation of diffusion creep.

Our conclusions are somewhat different from those by Wang *et al.* (*14*) on the $CaGeO_3$ perovskite and MgO analog system. They deformed their samples to less than 20% strain and found that $CaGeO_3$ perovskite is stronger than MgO by a factor of ~2. They concluded that the stronger phase $CaGeO_3$ perovskite controls the strength of the two-phase aggregate by comparing the results with the strength of pure $CaGeO_3$ perovskite.

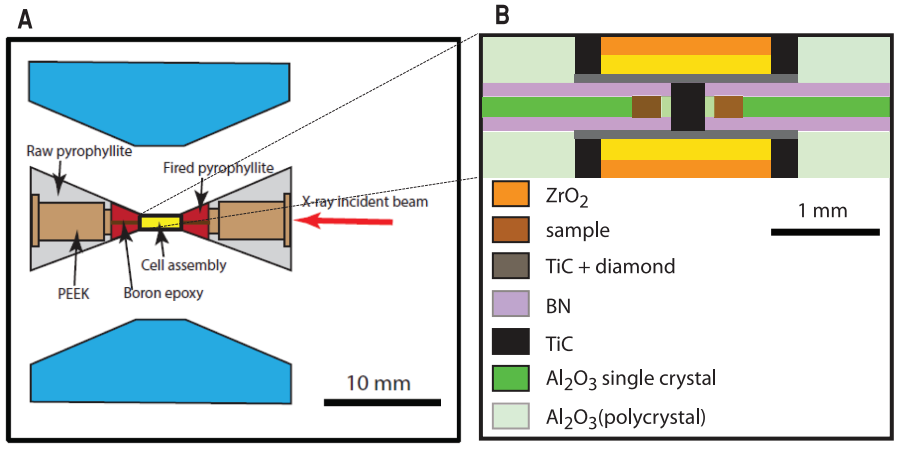

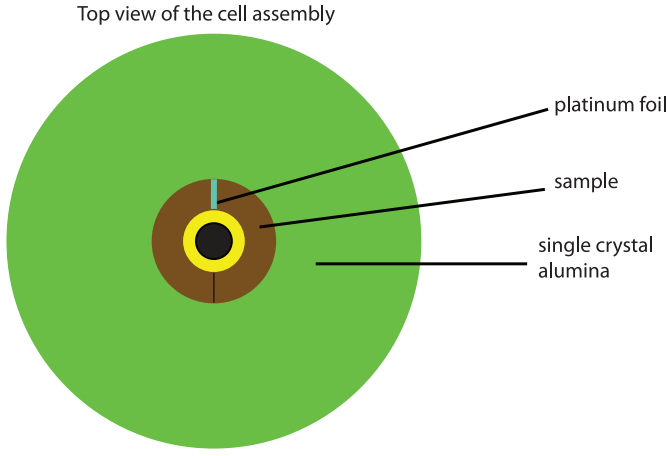

Fig. 1. The rotational Drickamer apparatus (RDA) cell assembly used to reach the shallow lower mantle conditions. (**A**) The anvils, gaskets, and cell assembly for the RDA deformation experiment; (**B**) a side view of the cell assembly; and (**C**) a top view of the cell assembly. Diffracted x-ray comes mostly from one side of a sample closer to the x-ray detectors.

Table 1. Summary of run conditions. The total strain is the equivalent strain, ε_E, including both axial compression strain (ε_U) and shear strain (ε_S) as $\varepsilon_E = \sqrt{\varepsilon_U^2 + \frac{4}{3}\varepsilon_S^2}$.

Run number	Temperature (K)	Pressure (GPa)	Total strain (%)	Strain rate ($\times 10^{-5}$ s^{-1})
beta 74*	2000 ± 100	24.1 ± 0.5	52	4.3
gamma 21*	2130 ± 100	27.0 ± 0.5	100	3.0
gamma 22	2130 ± 100	27.0 ± 0.5	55 ± 17	3.0 ± 0.9
gamma 23**	2140 ± 100	27.4 ± 0.5	0	0
gamma 24	2150 ± 100	27.5 ± 0.5	23 ± 7	3.2 ± 1.0
gamma 25	2150 ± 100	27.5 ± 0.5	48 ± 15	3.6 ± 1.1

*Strain marker was not visible in these runs. Strain was estimated from the angle of rotation of the anvil and the relationship between the angle of rotation and shear strain based on previous results. **After annealing, the furnace failed. No strain after annealing.

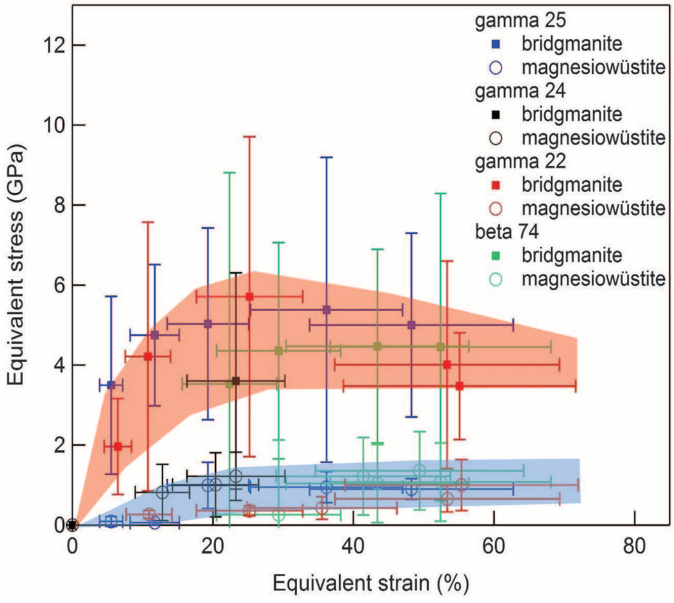

Fig. 2. A plot of the equivalent stress in bridgmanite and magnesiowüstite as a function of strain. Run conditions are given in Table 1. Stress in bridgmanite was estimated by using diffraction peaks (110) and (112). Stress in magnesiowüstite was estimated by using diffraction peaks (200) and (220). In both cases, the stresses shown here are the arithmetic average of stresses estimated from these planes. Some hint of strain weakening can be seen, particularly for bridgmanite (hatched regions are drawn to guide the eyes). Results from beta 74 are based on estimated strain (strain marker was not visible). Also, the pressure and temperature conditions for beta 74 are different from all others. Bars represent the errors. Errors are given for one standard deviation and are due to the uncertainties in the peak shift and the fitting errors to equation S1 (supplementary materials).

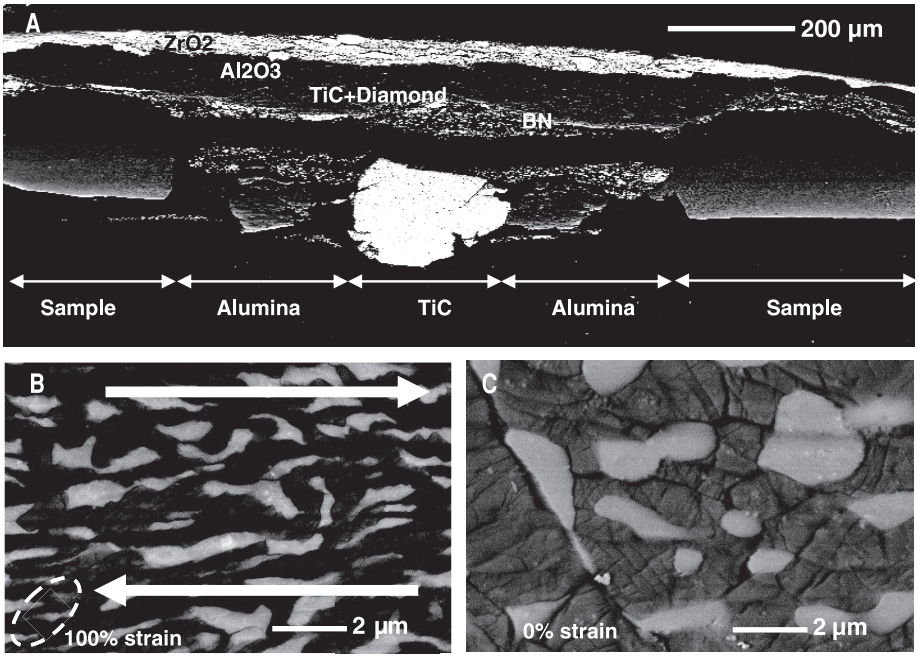

Fig. 3. SEM (scanning electron microscope) back-scattering images of the recovered sample from the run gamma 21. (**A**) A back-scattered electron image of the RDA cell assembly cut along the diameter. The sample position, alumina ring, and TiC central electrode are labeled for clarity. The layers of material above the sample are also identified (ZrO_2, Al_2O_3, TiC+Diamond, BN). (**B**) A back-scattered electron image of the recovered sample from the run gamma 21, deformed up to 100% strain. The light gray grains are mangesiowüstite, and the dark gray grains are bridgmanite. An oblate shape shows a strain ellipsoid corresponding to the bulk strain of 100%. Arrows indicate the sense of shear. (**C**) A back-scattered electron image of an undeformed sample from the run gamma 23. This sample was annealed at 27.4 GPa and 2140 K and quenched after 1.5 hours.

Although their observations on the strength contrast are similar to ours, we suggest that the larger strength contrast we observed for the lower mantle aggregate could promote shear localization more than an analog material where the strength contrast is less. Also, the difference in the strain magnitude may be responsible for the somewhat different results. Wang *et al.* (*14*) did not observe strain weakening but rather strain hardening at strain less than 20%. In that small strain regime, we also observed strain hardening. In contrast, we observed the hint of strain weakening at ~30% strain (Fig. 2). This suggests that the strength of the lower mantle aggregate could be controlled by a weaker phase at large strain. Similarly, a numerical study of deformation of a mixture of bridgmanite and magnesiowüstite by Madi *et al.* (*23*) showed no large strain partitioning to magnesiowüstite, but this study was made to very small strain (~10^{-4}).

We must examine the validity of the necessary extrapolation in strain rate (or stress level) from laboratory data to deformation in Earth. We conclude that dislocation creep dominates under the present experimental conditions on the basis of the large variation in stress estimated for different diffraction planes (*24*). Seismological observations of distribution of anisotropy suggest that dislocation creep may dominate in the boundary layers in the lower mantle (*25*). The stress dependence of strain rate in dislocation creep regime is similar between orthorhombic perovskite and magnesiowüstite (*26*, *27*). Consequently, the strength contrast between the two minerals deformed at geological strain rate would be similar to the contrast observed at laboratory strain rate in the boundary layer, where much of deformation occurs.

However, our current results contain major limitations, including (i) deformation mechanisms are not clearly identified, and the flow law was not determined in any detail; and (ii) the maximum strain is still low, and therefore the degree to which strain weakening could occur is unclear. In addition to well-characterized experimental studies to larger strains, characterization of strain weakening (and shear localization) may require numerical modeling, because small sample size might limit the full development of shear localization. The demonstration of significant stress-strain partitioning (and evolution) between the two major phases in the lower mantle, potentially resulting in shear localization, highlights the importance of experimental studies of deformation in interpreting geochemical and geodynamical observations.

REFERENCES AND NOTES

1. A. E. Ringwood, *Geochim. Cosmochim. Acta* **55**, 2083–2110 (1991).
2. A. W. Hofmann, *Nature* **385**, 219–229 (1997).
3. B. Marty, *Earth Planet. Sci. Lett.* **313-314**, 56–66 (2012).
4. U. R. Christensen, A. W. Hofmann, *J. Geophys. Res.* **99**, 19867–19884 (1994).
5. P. E. van Keken, E. H. Hauri, C. J. Ballentine, *Annu. Rev. Earth Planet. Sci.* **30**, 493–525 (2002).
6. S. Karato, D. J. Weidner, *Elements* **4**, 191–196 (2008).

7. H. Marquardt, L. Miyagi, *Nat. Geosci.* **8**, 311–314 (2015).
8. S. Merkel *et al.*, *Earth Planet. Sci. Lett.* **209**, 351–360 (2003).
9. S. Merkel *et al.*, *J. Geophys. Res.* **107**, 002002 (2002).
10. J. Chen, D. J. Weidner, M. T. Vaughan, *Nature* **419**, 824–826 (2002).
11. P. Cordier, T. Ungár, L. Zsoldos, G. Tichy, *Nature* **428**, 837–840 (2004).
12. S. Beauchesne, J.-P. Poirier, *Phys. Earth Planet. Inter.* **61**, 182–198 (1990).
13. S. Karato, *Phys. Earth Planet. Inter.* **55**, 234–240 (1989).
14. Y. Wang *et al.*, *Geochem. Geophys. Geosyst.* **14**, 3389–3408 (2013).
15. S. Karato, *Deformation of Earth Materials: Introduction to the Rheology of the Solid Earth* (Cambridge Univ. Press, Cambridge, 2008).
16. J. P. Bloomfield, S. J. Covey-Crump, *J. Struct. Geol.* **15**, 1007–1019 (1993).
17. S. Karato, *Phys. Earth Planet. Inter.* **24**, 1–14 (1981).
18. J. P. Poirier, J. Peyronneau, M. Madon, F. Guyot, A. Revcoleshi, *Nature* **321**, 603–605 (1986).
19. D. Yamazaki, S. Karato, *Rev. Sci. Instrum.* **72**, 4207–4211 (2001).
20. U. F. Kocks, *Metall. Trans.* **1**, 1121–1143 (1970).
21. M. R. Handy, *J. Struct. Geol.* **16**, 287–301 (1994).
22. S. Karato, S. Zhang, H.-R. Wenk, *Science* **270**, 458–461 (1995).
23. K. Madi, S. Forest, P. Cordier, M. Boussuge, *Earth Planet. Sci. Lett.* **237**, 223–238 (2005).
24. S. Karato, *Phys. Rev. B* **79**, 214106 (2009).
25. S. Karato, *Pure Appl. Geophys.* **151**, 565–587 (1998).
26. Z. Wang, C. Dupas-Bruzek, S. Karato, *Phys. Earth Planet. Inter.* **110**, 51–69 (1999).
27. T. G. Langdon, J. A. Pask, *Acta Metall.* **18**, 505–510 (1970).

ACKNOWLEDGMENTS

This study was supported by a grant from NSF. The experimental facilities at the Brookhaven National Laboratory are supported by the Department of Energy and COMPRES (Consortium for Materials Properties Research in Earth Sciences). We thank D. Weidner and H. Chen for the support at the synchrotron facility at Brookhaven National Laboratory. Z. Jiang provided technical support for the microstructural analyses. All data presented in this paper are available in the supplementary materials.

SUPPLEMENTARY MATERIALS

www.sciencemag.org/content/351/6269/144/suppl/DC1
Materials and Methods
Figs. S1 to S5
References (*28*–*41*)
Database S1

26 August 2015; accepted 12 November 2015
10.1126/science.aad3113

GEOMORPHOLOGY

Repeated catastrophic valley infill following medieval earthquakes in the Nepal Himalaya

Wolfgang Schwanghart,[1]* Anne Bernhardt,[1] Amelie Stolle,[1] Philipp Hoelzmann,[2] Basanta R. Adhikari,[3] Christoff Andermann,[4] Stefanie Tofelde,[1] Silke Merchel,[5] Georg Rugel,[5] Monique Fort,[6] Oliver Korup[1]

Geomorphic footprints of past large Himalayan earthquakes are elusive, although they are urgently needed for gauging and predicting recovery times of seismically perturbed mountain landscapes. We present evidence of catastrophic valley infill following at least three medieval earthquakes in the Nepal Himalaya. Radiocarbon dates from peat beds, plant macrofossils, and humic silts in fine-grained tributary sediments near Pokhara, Nepal's second-largest city, match the timing of nearby $M > 8$ earthquakes in ~1100, 1255, and 1344 C.E. The upstream dip of tributary valley fills and x-ray fluorescence spectrometry of their provenance rule out local sources. Instead, geomorphic and sedimentary evidence is consistent with catastrophic fluvial aggradation and debris flows that had plugged several tributaries with tens of meters of calcareous sediment from a Higher Himalayan source >60 kilometers away.

The M_w 7.8 Gorkha earthquake that struck Nepal in April 2015 confirmed high seismic risk projections for the Himalayas (*1*, *2*), inferred mostly from paleoseismological proxies of past events (*3*–*6*). Strong ground shaking caused the collapse of more than half a million homes, killing more than 8500 people and injuring more than 20,000. Landslides buried villages, roads, and river channels, consistent with coseismic impacts reported from other active mountain belts (*7*). Detailed sediment budgets show that landslides triggered by strong seismic ground shaking may rapidly detach millions to billions of cubic meters of rock, soil, and biomass, providing this material for subsequent entrainment by surface runoff and river flows (*8*). The resulting sediment pulses may fill even rapidly incising bedrock rivers by up to several tens of meters (*9*), thereby causing protracted channel instability, impeding access to emergency areas, destroying hydropower facilities, and compromising post-disaster rehabilitation efforts. Detailed mass balances of recent large earthquakes in China (*10*), Taiwan (*11*), Japan (*12*), and New Zealand (*13*) offer blueprints of how river networks recover from sudden input of excess sediment over several years to centuries. The high sediment transport rates in many mountain rivers, however, rarely sustain evidence of prehistoric earthquake-induced sedimentation pulses. In these cases, depositional records of catastrophic aggradation in forelands are more instructive (*14*). Both of these lines of evidence for understanding river network recovery have remained elusive in the Himalayas. We present exceptionally well-preserved sedimentary archives that connect landscape-scale disturbance around Pokhara, Nepal, to at least three documented medieval megathrust earthquakes (*3*).

The city of Pokhara (28°13′N, 83°59′E, 870 m above sea level) is located at the foot of the >8000-m peaks of the Annapurna Massif in the Seti Khola valley (Fig. 1). This steep orographic gradient receives monsoonal rainfall of ~4000 mm year^{-1} (*15*). Pokhara's geology features primarily Precambrian metamorphic sandstones, shales, and dolomites. Other rocks include Paleozoic phyllites and schists of the Lesser Himalayan Series (LHS). Higher Himalayan Crystalline (HHC) rocks north of the Main Central Thrust (MCT) are Precambrian high-grade metamorphic quartzites, schists, and gneisses (*16*, *17*). Marine calcareous metasediments of the Tethyan Sedimentary Series (TSS) prevail north of the South Tibetan Detachment Zone (*18*, *19*). Pokhara sits on a large sediment fan built by the upper Seti Khola that drains the partly glaciated and debris-filled Sabche Cirque in the Annapurna Massif. The fanhead near the MCT grades into a ~60-km-long flight of prominent terraces downstream that rise up to 140 m above the river bed and envelop several LHS bedrock hills (*20*). The fan has three stratigraphic units called the Tallakot, Ghachok, and Pokhara Formations. We focus on the youngest Pokhara Formation composed of extensive coarse gravel sheets, numerous boulders >10 m in diameter, and thick debris flow deposits. Digital topographic data (*21*) confirm damming of the more than a dozen tributaries along Seti Khola's course of >60 km by Pokhara Formation sediments (*20*). These deposits dip upstream into tributary valleys for >1 km and up to 7 km along the Magdi and Saraudi Khola featuring several meters of intercalated gravel, sand, and silt beds. We sampled enclosed peat beds, charcoal lenses, and plant macrofossils (figs. S1 and S2) for radiocarbon (^{14}C) dating and for any earthquake-related sedimentation in eight different tributaries (table S1).

Bayesian calibration of 26 ^{14}C ages with a prior informed by stratigraphic relationships between the samples (*22*) returned a pooled posterior distribution with three distinct peaks that match, within error, the timing of three large medieval earthquakes in ~1100, 1255, and 1344 C.E. (*3*–*5*) (Fig. 2, figs. S3 to S5, and table S2). Our oldest ^{14}C dates offer support for the timing of the ~1100 C.E. earthquake, which has so far been inferred from

[1]Institute of Earth and Environmental Science, University of Potsdam, Potsdam, Germany. [2]Institute of Geographical Sciences, Freie Universität Berlin, Berlin, Germany. [3]Institute of Engineering, Tribhuvan University, Kathmandu, Nepal. [4]Helmholtz-Zentrum Potsdam, German Centre for Geosciences GFZ, Germany. [5]Helmholtz-Zentrum Dresden-Rossendorf, Helmholtz Institute Freiberg for Resource Technology, Dresden, Germany. [6]CNRS UMR 8586 Prodig, Département de Géographie, Université Paris-Diderot-SPC, Paris, France.
*Corresponding author. E-mail: w.schwanghart@geo.uni-potsdam.de

Shear deformation of bridgmanite and magnesiowüstite aggregates at lower mantle conditions

Jennifer Girard, George Amulele, Robert Farla, Anwar Mohiuddin and Shun-ichiro Karato

Science **351** (6269), 144-147.
DOI: 10.1126/science.aad3113originally published online December 31, 2015

Mantle minerals won't share the strain

The deformation of a mixed block of material depends on the strength of the components of which it is made. Weak materials will deform more than the strong ones in a mixture that is squished or stretched. Girard *et al.* find a large difference in strength between the two primary minerals making up Earth's lower mantle (see the Perspective by Chen). Deformation in the convecting mantle may occur only near boundary layers as a result, leaving large regions potentially unaffected. This could explain long-lived chemical reservoirs in Earth's interior and the lack of seismic anisotropy in the lower mantle.

Science, this issue p. 144; see also p. 122